Bio-Design and Manufacturing (2021) 4:243–257
https://doi.org/10.1007/s42242-020-00113-4

RESEARCH ARTICLE

Reduced graphene oxide-grafted bovine serum albumin/bredigite nanocomposites with high mechanical properties and excellent osteogenic bioactivity for bone tissue engineering

Esfandyar Askari[1,2] · Mohammad Rasouli[1] · Seyedeh F. Darghiasi[1] · Seyed M. Naghib[1] · Yasser Zare[2] · Kyong Y. Rhee[3]

Received: 21 July 2020 / Accepted: 13 November 2020 / Published online: 6 January 2021

Abstract

The optimization of the scaffolds to provide a suitable matrix and accelerate the regeneration process is vital for bone tissue engineering. However, poor mechanical and biological characteristics remain the primary challenges that must be addressed. For example, although bredigite (Br) has shown great potential for application in bone tissue engineering, it easily fails in replacement. In the present work, these challenges are addressed by reinforcing the Br matrix with nanosheets of graphene oxide (rGO) that have been reduced by bovine serum albumin (BSA) in order to enhance the mechanical properties and biological behavior. The reduction of graphene oxide by BSA improves the water stability of the nanosheets and provides an electrostatic interaction between the BSA-rGO nanosheets and the Br particles. The high thermal conductivity of the BSA-rGO nanosheets decreases the porosity of the Br by transferring heat to the core of the tablet. Furthermore, the addition of BSA-rGO nanosheets into the Br matrix enhances the adhesion of G-292 cells on the surface of the tablets. These findings suggest that the tablet consisting of BSA-rGO-reinforced Br has encouraging potential for application in bone tissue engineering.

Keywords Bovine serum albumin (BSA) · Reduced graphene oxide (rGO) · Bredigite · Mechanical properties · Bone tissue engineering

Introduction

Bone tissue engineering represents an alternative approach for repairing and regenerating broken hard tissue that avoids the need for the regular re-implantation of biomaterials [1–3]. The bioactivity of biomaterials is critical for stimulating the requisite cell and tissue growth for promoting reconstruction of the extracellular matrix (ECM) and supporting the regeneration of hard tissue [4–7]. In particular, the calcium silicate bio-ceramics have attracted much attention for developing the requisite bioactive responses for the regeneration, repair, and remodeling of bone tissue affected by trauma [8]. Alternatively, the silicate-based bio-ceramics are suitable bioactive materials for promoting bone tissue ingrowth when used in composites or coatings [9–11]. An important example is the calcium–silicate–magnesium mineral bredigite (Br), which belongs to the $Ca_7MgSi_4O_{16}$ system. Recent findings have demonstrated the significant bioactivity of this bio-ceramic system over the connective bone cells with the potential to promote not only osteo-conductivity, osteo-inductivity, and osteogenesis, but also osteo-regeneration due to the apatite-forming capability provided by the presence of calcium, silicate, and magnesium [12]. In particular, the afore-mentioned rapid apatite formation, superb biocompatibility, excellent osteo-inductivity (which facilitates robust

Esfandyar Askari, Mohammad Rasouli, and Seyedeh F. Darghiasi have equally contributed to this work as the first authors.

✉ Seyed M. Naghib
naghib@iust.ac.ir

✉ Kyong Y. Rhee
rheeky@khu.ac.kr

1 Nanotechnology Department, School of Advanced Technologies, Iran University of Science and Technology (IUST), P.O. Box 16846-13114, Tehran, Iran

2 Biomaterials and Tissue Engineering Research Group, Department of Interdisciplinary Technologies, Breast Cancer Research Center, Motamed Cancer Institute, ACECR, Tehran, Iran

3 Department of Mechanical Engineering, College of Engineering, Kyung Hee University, Yongin 446-701, Republic of Korea

stimulation of osteoblast proliferation), and high osteogenic bioactivity have been attributed to the silicon component of this bio-ceramic [13–15]. Moreover, the mechanical characteristics of Br are very similar to those of cortical bone tissue [16, 17], thus enabling the Br to support various mechanical loads and making this material a more appropriate choice than other bioactive ceramics such as hydroxyapatite or tricalcium phosphate [18].

Due to their exceptional physicochemical, electrical, mechanical, and biological features, as well as their bioactivity and cytocompatibility [8], graphene-based nanosheets and their derivatives have recently gained a great deal of attention for applications in theranostics [19], biosensing [20], tissue engineering [21], imaging [22], lab-on-a-chip [23], cancer detection [24] and controlled release of therapeutic molecules [25, 26]. Several critical characteristics, including high surface area, enhanced electroconductivity, the presence of oxygen-containing functional groups, and cytocompatibility in the presence of normal cells, have established graphene as a unique nanosheet for biomedical applications. In particular, cytocompatibility and fast functional bioactivity have established the graphene-based nanomaterials and nanocomposites as promising platforms in cancer therapy, the delivery of therapeutic molecules, tissue regeneration, imaging, and biosensing. In addition to the afore-mentioned biosensing applications, their chemical characteristics make them applicable for the management of hypothermia [27]. Further, graphene-mediated nano-biomaterials are utilized in hard tissue engineering and bone regeneration [8]. Both graphene oxide (GO) and reduced graphene oxide (rGO) are exploited in osteogenic bioactivity of various stem cells to investigate neurogenesis [28], adipogenesis [29], myogenesis [30], epithelial genesis [31], cardiomyogenesis [32], and chondrogenesis [33]. Furthermore, the graphene-based nanomaterials can be modified in order to tailor their cytocompatibility, solubility, and selectivity in biological and physiological systems [31]. In addition, graphene-mediated nanomaterials and nanocomposites are broadly exploited in antibacterial applications [34], cancer-targeting [35], antiviral therapies [36], and energy storage [37]. Recently, graphene-based nanofillers have been widely exploited in the forms of GO, graphene nanoplatelets, and rGO, for improving the mechanical properties of bio-ceramics and bioactive ceramics such as zirconia/alumina composites [38], hydroxyapatite [39], alumina (Al_2O_3) [40], and silicon nitride (Si_3N_4) [41]. Most graphene-grafted bio-ceramic nanocomposites display decreased fracturing due to crack tip shielding, crack deflection, crack branching, and crack bridging [8]. In addition, Li et al. used spark plasma sintering to fabricate a nanoscaled hydroxyapatite on a chitosan–GO composite with a demonstrable improvement in biocompatibility [42]. Similarly, Zhang et al. synthesized graphene nanoplatelets–hydroxyapatite nanocomposites with good mechanical characteristics, cytocompatibility, excellent osteo-conductivity, and apatite-forming capacity in comparison with pristine hydroxyapatite [43]. In recent years, rGO has appeared as a competitive nanosheet compared to graphene due to its superior physicochemical and biological properties. For example, Mehrali et al. used a hydrothermal method and hot isostatic pressing to prepare rGO-reinforced calcium silicate nanocomposites with excellent mechanical characteristics, cell proliferation, osteo-inductivity, and osteogenic bioactivity [8].

In the present paper, the synthesis of a mechanically enhanced scaffold consisting of BSA-reduced graphene oxide nanosheets and Br particles is described. The BSA is shown to stabilize and reduce the graphene oxide nanosheets to create an electrostatic interaction between the rGO nanosheets and the Br particles. The structure of the resulting Br-decorated BSA-rGO nanosheets is examined by field emission scanning electron microscopy (FESEM) and confirmed by Raman spectroscopy. In addition, thermal conductivity measurements indicate that the porosity of the BSA-rGO incorporated Br tablet is considerably reduced. Moreover, the strong bonding between the BSA-rGO nanosheets and the Br particles is found to enhance greatly the hardness of the nanocomposite. Finally, the incorporation of the Br particles into the BSA-rGO nanosheet matrix is shown to enhance the adhesion of osteoblast-like cells, thus suggesting that this composite is mechanically and biologically appropriate for bone tissue engineering applications.

Materials and methods

Materials

The BSA, the raw materials for the synthesis of Br, namely magnesium nitrate hexahydrate ($Mg(NO_3)_2.6H_2O$), calcium nitrate tetrahydrate ($Ca(NO_3)_2.4H_2O$), and tetraethyl orthosilicate ($(C_2H_5O)_4Si$, TEOS), and those for the synthesis of GO, namely sulfuric acid (H_2SO_4), graphite (C), hydrogen peroxide (H_2O_2), and potassium permanganate ($KMnO_4$), were purchased from Merck and used without any purification. The G292 clone A141B1 cells (osteoblast-like cells) were purchased from the Pasteur Institute of Iran (Iran National Cell Bank, Tehran, Iran). Finally, the penicillin–streptomycin mixture (Pen-Strep), fetal bovine serum (FBS), Dulbecco's modified Eagle's medium (DMEM), and trypsin were purchased from Gibco (UK).

Br synthesis

Pure Br was synthesized using magnesium nitrate hexahydrate, TEOS, and calcium nitrate tetrahydrate by the

sol–gel method. First, water was mixed with TEOS and 2 M nitric acid in the mol ratio of 4:1:0.08 (H_2O:TEOS:HNO_3) and the solution was stirred for 30 min for the hydrolysis reaction to proceed. This was followed by the addition of magnesium nitrate hexahydrate and calcium nitrate tetrahydrate in the mol ratio of 7:4:1 ($Ca(NO_3)_2.4H_2O$:TEOS:$Mg(NO_3)_2.6H_2O$). The solution was stirred at 23 °C for 5 h, held at 60 °C for a further 24 h, and then dried for 48 h in an oven at 120 °C to obtain the gel. Finally, the dried gel was calcined in a furnace at 1150 °C for 3 h [44].

Graphene oxide synthesis

GO was synthesized by a modification of Hummer's method that avoids the use of sodium nitrate ($NaNO_3$) by using hydrogen peroxide (H_2O_2) along with sulfuric acid (H_2SO_4), graphite, and potassium permanganate ($KMnO_4$). In detail, graphite powder (3.0 g) was combined with H_2SO_4 (70 ml) and stirred in an ice bath to control the temperature. This was followed by the gradual addition of $KMnO_4$ (9.0 g), taking care that the temperature of the solution did not rise above 20 °C. The solution was then moved to a pre-heated oil bath and stirred vigorously for 30 min at 40 °C. At that time, 150 ml of water was added to the solution, followed by stirring at 95 °C for 15 min. A further 500 ml of water, along with 15 mL of H_2O_2 (30%), was then added until the solution turned from dark brown to yellow. The metal ions were then removed by washing the solution with a 1:10 HCl aqueous solution (250 ml), filtering, and drying at room temperature the obtain the solid [45].

Reduction of GO nanosheets using BSA

The synthesized graphene oxide nanosheets were dispersed in the deionized water by probe-ultrasonication (25 W, 2 h). The BSA powders were added to the GO solution in a 250 mg:50 mg ratio (BSA:GO). The pH of the solution was adjusted to the optimum conditions using NaOH (1 molar). The reduction process was performed under vigorous stirring overnight. Importantly, the temperature of the solution was maintained at 65 °C using a water bath.

BSA-rGO–Br ceramic composite synthesis

Three mixtures with various contents of Br/BSA-rGO (0.5, 1.0, and 2.0 wt%) were prepared (Table 1). For example, 0.5 wt% BSA-rGO–Br composite was prepared by dissolving BSA-rGO (0.01 g) in 96% ethanol (25 ml). The solution was mixed by ultrasonication for 2 h, followed by the addition of Br (2 g) and a further 2 h of ultrasonication. This solution was then stirred for 24 h, followed by centrifugation for 5 min at 2000 rpm and drying in an oven at 85 °C for 24 h [46]. Samples of the pure Br and BSA-rGO–Br powders were then pressed into tablet. The tablets sintered at 1250 °C for 3 h. In this process, stability of tablets was enhanced and stored for further characterizations.

Table 1 The component of Br and Br/BSA-rGO composite samples

Br/BSA-rGO (wt%)	Br (g)	BSA-rGO (g)
0.5	2	0.01
1	2	0.02
2	2	0.04

Characterization

To characterize the Br–BSA-rGO, BSA-rGO, and Br powders, Raman spectroscopy was performed using a Renishaw Invia Raman Microscope with a 514 nm laser, and field emission scanning electron microscopy (FESEM) was performed using a high-resolution FEI Quanta 200F instrument in combination with energy dispersive X-ray (EDX) spectroscopy (Hitachi, S-4800) to determine the chemical compositions. In addition, the functional groups present in the composites were identified by Fourier transform infrared spectroscopy (FTIR) using a PerkinElmer System (USA) in the frequency range of 4000–400 cm^{-1} [47]. The phase composition and structure of the powders were identified by XRD analysis using a Philips diffractometer (30 mA, 40 kV) and monochromated CuKα radiation (wavelength = 0.15406 nm) in the 2θ range of 10–90° with a step size of 0.05 degree/second. The resulting XRD patterns were analyzed using the PANalytical X'Pert Highscore software. In addition, the surface charges and particle size distributions of the Br and BSA-rGO powders were determined by zeta-potential analysis (Zeta sizer Nano series, Nano ZS90, UK) [48]. The crystallite size of the Br powders was determined using the Williamson–Hall equation, as given by Eq. 1:

$$B\cos\theta = 0.89\lambda/D + 2A\sqrt{\varepsilon^2}\sin\theta, \quad (1)$$

where B is the full width at half maximum (FWHM) of the diffraction peaks, λ is the X-ray wavelength employed (λ = 0.15406 nm), D is the average crystallite size, ε is internal lattice strain, θ is the diffraction angle, and A is a coefficient depending on the strain distribution. Finally, the phase transformation of the bio-ceramic powder was tracked via simultaneous thermogravimetric and differential thermal analysis (TG–DTA) measurements using a thermal analyzer (STA 504, TA Instruments) [44].

Microhardness testing

Microhardness of the sintered tablets was evaluated by means of a Vickers microhardness tester (HMV-2, Shimadzu Corpo-

ration, Japan). A pyramidal diamond indenter was utilized to the tablets surface under various loads of 0.0856 N, 0.2387 N, and 0.4956 for 15 s, respectively. Diagonal length of the indentation was measured by using a micrometric eyepiece with an objective lens of 40 × in hardness test was repeated 7 times on different locations of tablets.

Cell culture

The G292 (osteoblast like) cells were cultured in DMEM supplemented with 1% Pen-Strep and 10% (v/v) FBS, then incubated under a 5% humidified CO_2 atmosphere at 37 °C [46]. To harvest the cells for subsequent use, trypsin (0.25%) was used to suspend the cells from the culture dish wall until the cell confluence reached approximately 85%.

Cell adhesion

The G292 (osteoblast like) cells were seeded in a 12-well plate with the various wt% Br-rGO tablets. The cultured cells on the sample surface were then treated with glutaraldehyde (4%) at 25 °C for 120 min, washed three times with a phosphate buffer saline solution (PBS, 0.1 M), then dehydrated with graded solutions of water/ethanol (40, 50, 60, 70, 80, 90, and 100%, respectively). To maintain the original cell morphology, hexamethyldisilazane (HMDS, 0.5 mL) was added to each well. Finally, the samples were placed in a fume hood at 25 °C to dry.

Washout property test

To measure the washout property, tablets with 10 mm diameter and 2 mm thickness were fabricated. The tablets (in PBS) were statically placed in an incubator at 37 °C and 95% relative humidity for 72 h. The washout mass ratio was calculated by:

$$\text{Washout mass ratio} = \frac{\text{The final weight of the remaining tablets on the net}}{\text{The weight of whole tablet sample}}.$$

MTT assay

The G292 (osteoblast like) cells were cultured in DMEM supplemented with 1% Pen-Strep and 10% (v/v) FBS, incubated under a 5% humidified CO_2 atmosphere at 37 °C for 2 days. The cells were then collected, seeded into each well of a 12-well plate at a density of 1×10^4, and cultured in DMEM supplemented with FBS (10%). The medium with FBS (10%) without tablets was utilized as a negative control. After each incubation for 1, 3 and 7 days, 0.5 mg/ml of 3-(4,5-dimethylthiazol-2-yl)-2,5-diphenyl tetrazolium bromide (MTT) solution was added to every well. After 4 h of incubation, dimethyl sulfoxide (DMSO) was added to stop the reaction between the cells and the MTT. Eighty microliters of medium of samples was separated in triplicate and transferred to 96-plate. The optical density (OD) was calculated at 570 nm wavelength using an Aliza plate reader (Bio Tek Instruments, USA) [46].

ALP activity

The alkaline phosphatase (ALP) activity was measured using the appropriate kit (Parsazmun, Iran) according to the manufacturer's protocol. Briefly, the G292 (osteoblast-like cells (5×10^3) were seeded on Br and BSA-rGO–Br tablets in a 24-well plate and cultured for 1, 3, or 7 days. Then, 20 µl aliquots of each well supernatants were diluted and mixed with the kit solution. All of the samples were repeated triplicate. The Aliza plate reader was used to evaluate the adsorption changes at 405 nm and 23 °C [46, 49].

Statistical analysis

Measurements were represented as the mean ± standard deviation (SD) and were tested using the Student's T test. Analyses were performed using the GraphPad Prism software, and p values < 0.05 were considered to be statistically significant [48].

Result and discussion

Br characterization

The SEM image in Fig. 1a reveals the surface morphology and microstructure of the Br, with the sizes of individual and agglomerated particles ranging from 1 to 10 µm. Meanwhile, the XRD pattern of the Br powder after heat treatment at 1150 °C in Fig. 1b displays an intense diffraction peak at $2\theta = 32.23°$, corresponding to a d-spacing of 2.77 nm. In addition, the crystallite size of the Br powder was determined by the Williamson–Hall equation to be approximately 35.3 nm.

The crystal system of the Br has been reported to be orthorhombic with cell parameters in the ratio of a:b:c = 0.594:1:0.367 [44]. It is widely known that the behavior of the bio-ceramics during heat treatment is a significant indicator of their suitability for biological applications. In other words, thermal analysis can be used to effectively determine the extent of removal of any toxic by-products and the structural development of the bio-ceramics in order to demonstrate that the bio-ceramics have their optimum efficiency. Therefore, in the present study, thermal analysis was conducted on the synthesized powder sample.

The corresponding DTA and differential DTA graphs (Fig. 1c) reveal the appearance of an endothermic peak at

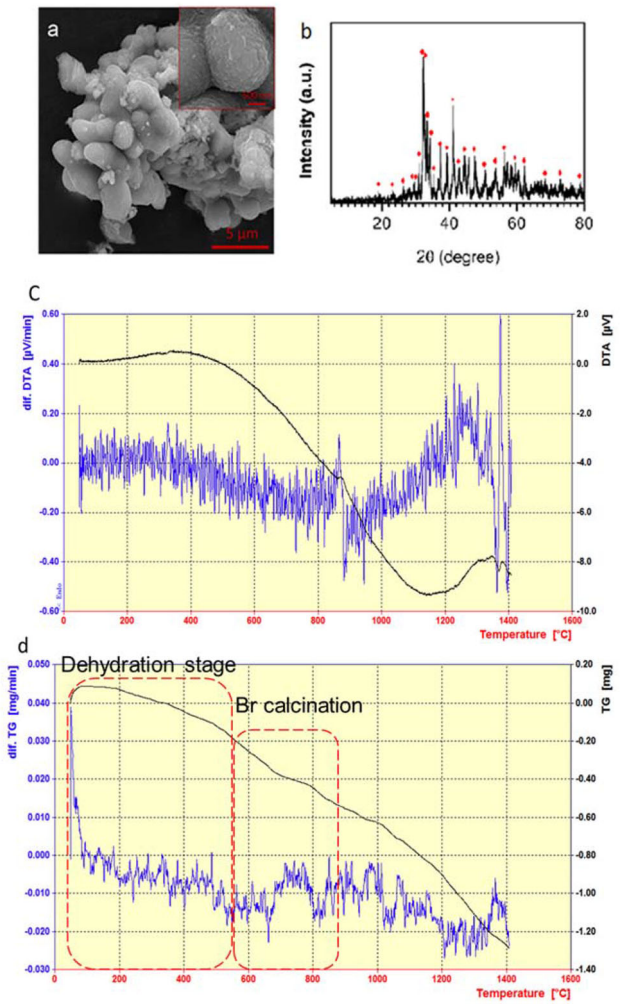

Fig. 1 SEM (**a**), XRD (**b**), dif. DTA and DTA (**c**), dif. TG and dif. DTA (**d**) of the Br synthesized by the sol–gel method that was calcined at 1150 °C

around 385 °C, which is related to the release of nitrite from magnesium nitrite, and a second exothermic peak at 870 °C, which is related to the initiation of Br calcination [50]. The TG and differential TG traces of the Br powder are presented in Fig. 1d. Here, the powder weight loss is seen to have occurred in two main stages, with the first stage (below 580 °C) being related to dehydration of the powder and the second stage (between 580 and 870 °C) being related to calcination of the Br. *BSA-rGO*. These processes are marked as red lines in Fig. 1d [9, 51].

The Raman spectra in Fig. 2a were acquired in order to assess the graphene structure in the various powders. Here, the excellent quality of the GO product is revealed by the presence of the G band at 1570 cm^{-1}, the 2D band at 2700 cm^{-1}, and the D band at 1350 cm^{-1}. For the GO, the intensity ratio of the D band to that of the G band (I_D/I_G) is found to be 1/15, thus indicating the high level of graphene oxidation [19]. In the Raman spectrum of the BSA-rGO, the appearance of the D band demonstrates that the vibration occurred in a hexagonal carbon lattice. Moreover, the I_D/I_G ratio of 1.18 indicates an increase in the level of sp^3 hybridization due to the attachment of the functional groups [52]. Meanwhile, the FTIR spectra of the GO and BSA-rGO powders are presented in Fig. 2b. Here, the GO spectrum (blue curve) exhibits the following adsorptions: 990 cm^{-1} and 1100 cm^{-1}, which are attributed to the C–O–C tensile vibration; 1500 cm^{-1} and 1600 cm^{-1}, corresponding to the stretching vibration of the benzene framework; 1800 cm^{-1} due to the C=O tensile vibration; and 3400 cm^{-1} due to the O–H tensile vibration with hydrogen bonding. Meanwhile, the BSA-rGO spectrum reveals the appearance of a peak at 540 cm^{-1} corresponding to the O=C–NH in-plane bending vibration, while the carbonyl peak is replaced by a peak at 1600 cm^{-1} due to the cross-linking of amide groups with O=C–OH [52].

This indicates that the amine groups of the BSA were successfully grafted onto the GO surface. In addition, the appearance of a peak at 2950 cm^{-1} is related to the C-H tensile vibrations of the BSA methylene group. Briefly, the formation of the BSA-rGO composite is suggested by the appearance of the predominant peaks at 2950 cm^{-1} and 540 cm^{-1} in the spectrum of BSA-rGO, in contrast to that of the GO powder [53]. The successful formation of BSA-rGO nanosheets is also indicated by the FESEM image in Fig. 2c. Moreover, as can be seen in Fig. 2d, a slightly wrinkled single- and double-layer lamellar structure of the BSA-rGO nanosheets was established, with the size of the lamellar structure being about 1 µm.

Structural analysis of graphene-reinforced Br

Any enhancement in the desired features of a composite is strongly dependent upon the interfacial interaction between the matrix and the filler; hence, this is an important parameter in composite formation. In previous work [52], we demonstrated that BSA-decorated graphene displays a switchable electrostatic charge at various pH values In the present work, the zeta potentials of the BSA-rGO and Br powders demonstrate that the electrostatic interaction between the positively charged BSA-rGO nanosheets and negatively charged Br particles provides suitable interfacial bonding (Fig. 3).

Meanwhile, the dispersion of Br particles on the surface of the BSA-rGO nanosheets is demonstrated in Fig. 4a and b, while the existence of the BSA-rGO nanosheets themselves is confirmed by Raman spectroscopy (Fig. 4c). Graphene and related materials generally display D, G and 2D peaks in their Raman spectra. Thus, in Fig. 4c, the BSA-rGO spectrum exhibits a D band at 1349 cm^{-1} due to the in-plane C–C bond stretching in graphene, while the G band is located at 1595 cm^{-1} due to the presence of defects in the structure [52, 54]. The existence of D and G bands in the BSA-rGO–Br

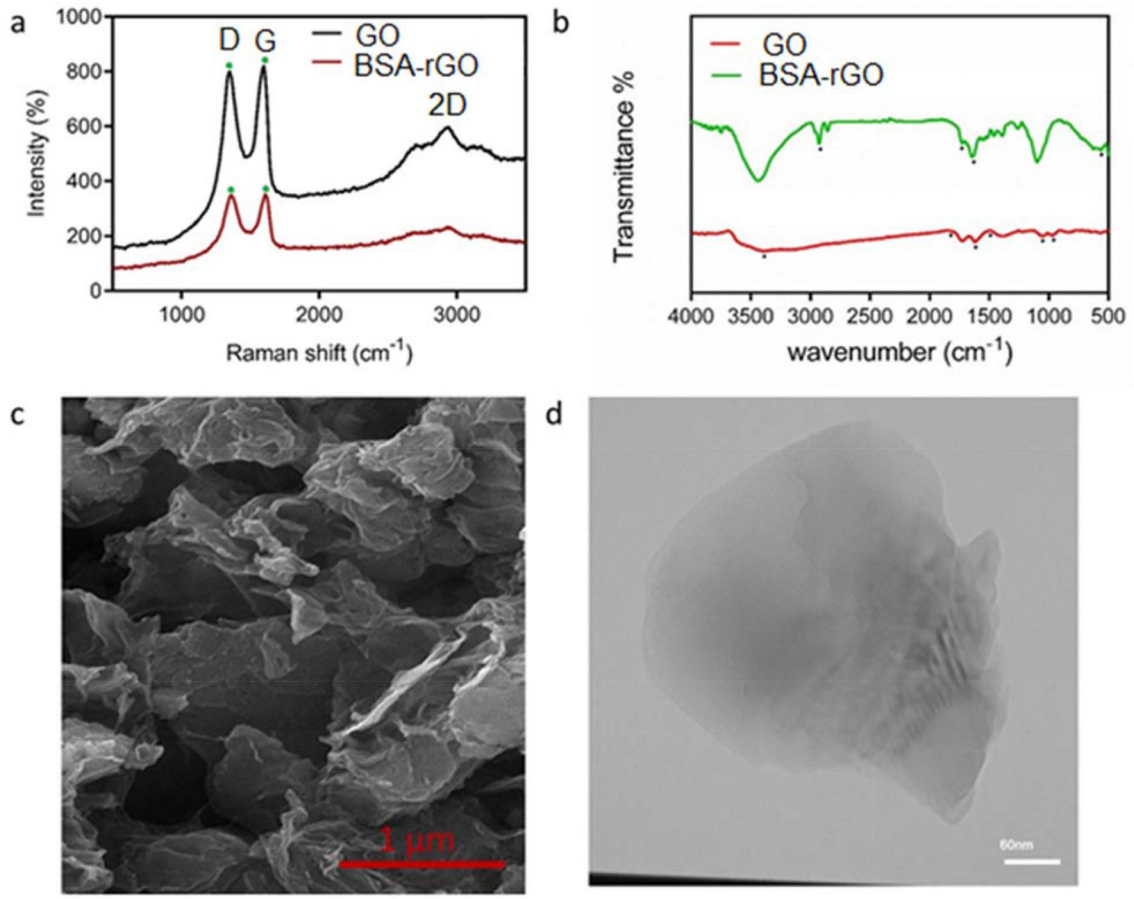

Fig. 2 Raman spectroscopy analyses of GO and BSA-rGO (**a**), FTIR of GO and BSA-rGO (**b**), FESEM (**c**), and TEM of BSA-rGO (**d**)

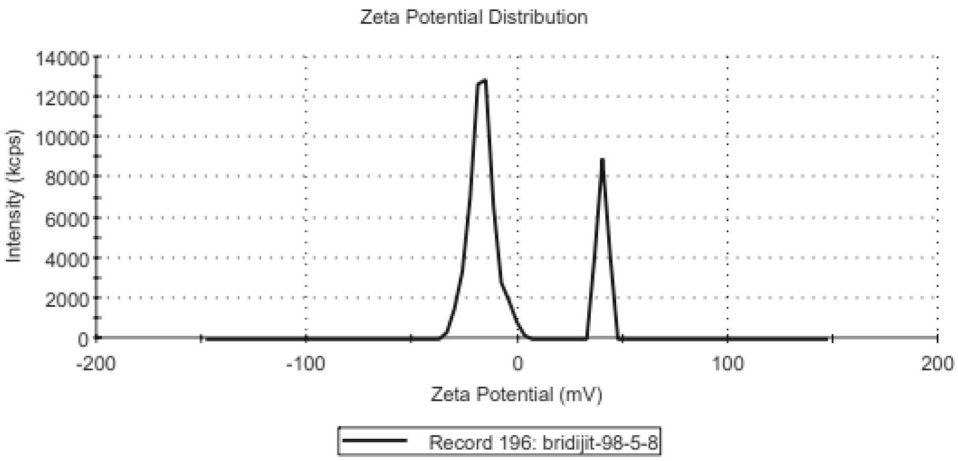

Fig. 3 Zeta potential of Br particles

nanocomposite confirmed the persistence of the graphene nanosheets after enduring the harsh processing conditions. In addition, significant blue shifts (i.e., shifts to higher frequency) of ~ 23 and 18 cm^{-1} were observed for the D and G bands after the addition of graphene to the Br. This was primarily due to the compressive stress applied during the tablet formation process. Moreover, in Fig. 4c, the I_D/I_G ratio is seen to be higher for the BSA-rGO–Br than for the BSA-rGO, thus demonstrating the introduction of some structural defects into the graphene during the composite formation process. This observation is in agreement with our previously reported work [43].

The general challenge in bio-ceramics has been that of agglomeration leading to decreased dispersion capability.

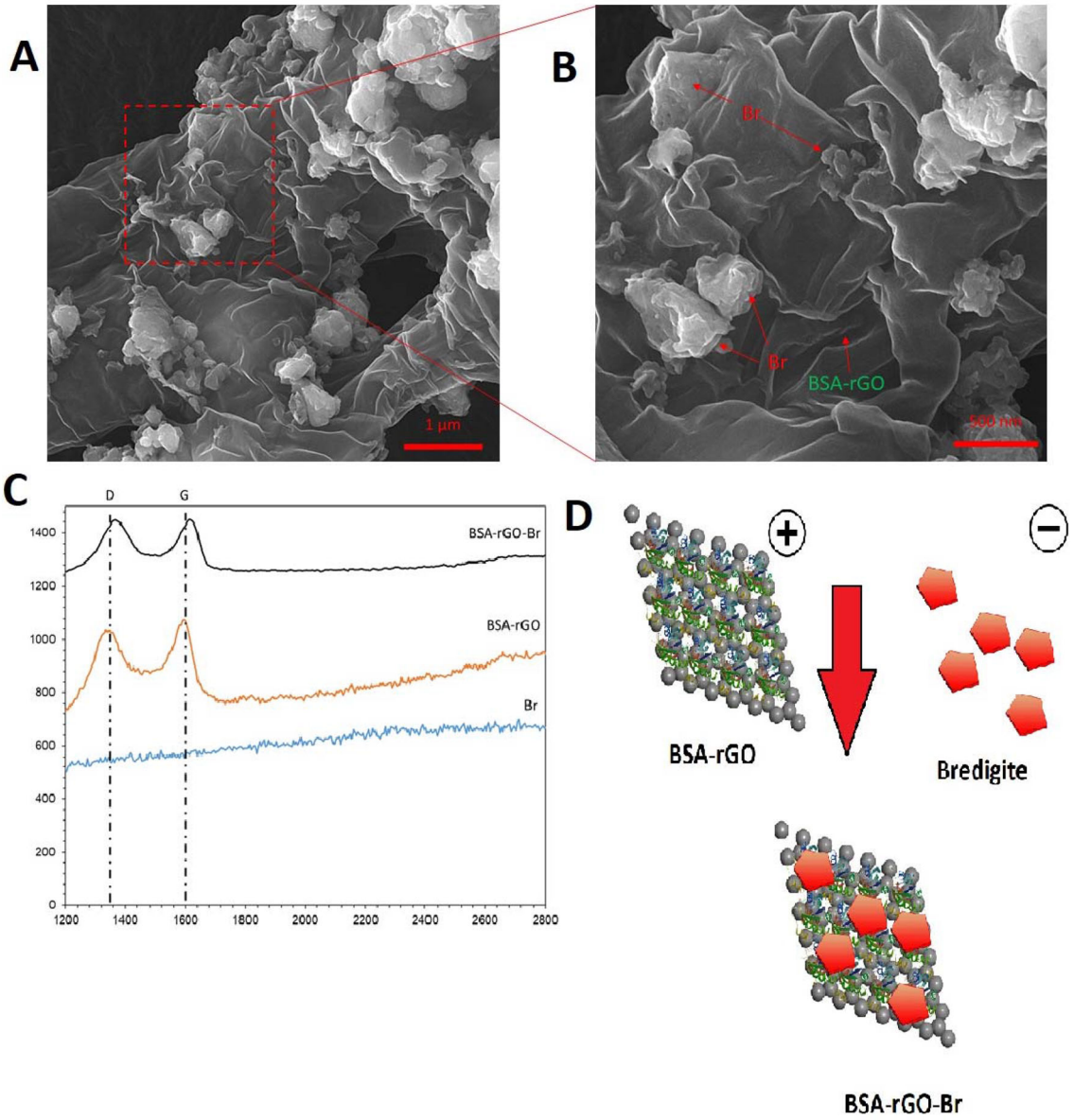

Fig. 4 Interaction between BSA-rGO nanosheets and Br particles: SEM images in the zoom out and zoom in mood illustration of the Br particles deposition on the surface of BSA-rGO nanosheets (**a** and **b**), Raman spectrum of Br, BSA-rGO and BSA-rGO–Br (**c**) and schematic presentation of electrostatic interaction between nanosheets and microparticles (**d**)

Thus, in the present study, the observed semi-uniform dispersion of Br particles on the surface of the BSA-rGO nanosheets provides evidence for a decrease in the rate of agglomeration of the Br particles. This is because the BSA that was used to reduce and stabilize the graphene nanosheets created active sites that could absorb the Br particles and, thus, inhibit aggregation of the bio-ceramic particles [55, 56]. In fact, due to the positively charged residues that were decorated on the surface of GO nanosheets, BSA-rGO nanosheets could co-assembled with some negatively charged materials by mutual electrostatic interaction. As can be seen in Fig. 4d, this interaction generated a sandwich-like structure in which polygonal Br particles were dispersed in the BSA-rGO nanosheet layers.

The phase compositions of the BSA-rGO–Br, the BSA-rGO, and the Br are compared by the XRD patterns in Fig. 5a. As mentioned in the previous section, the Br crystallite structure and phase composition were confirmed by the previously reported literature. In Fig. 5a, it can be seen that the addition of BSA-rGO into the Br does not alter the phase composition of the matrix. While the low concentration of graphene filler in the matrix leads to the absence of a graphene-related

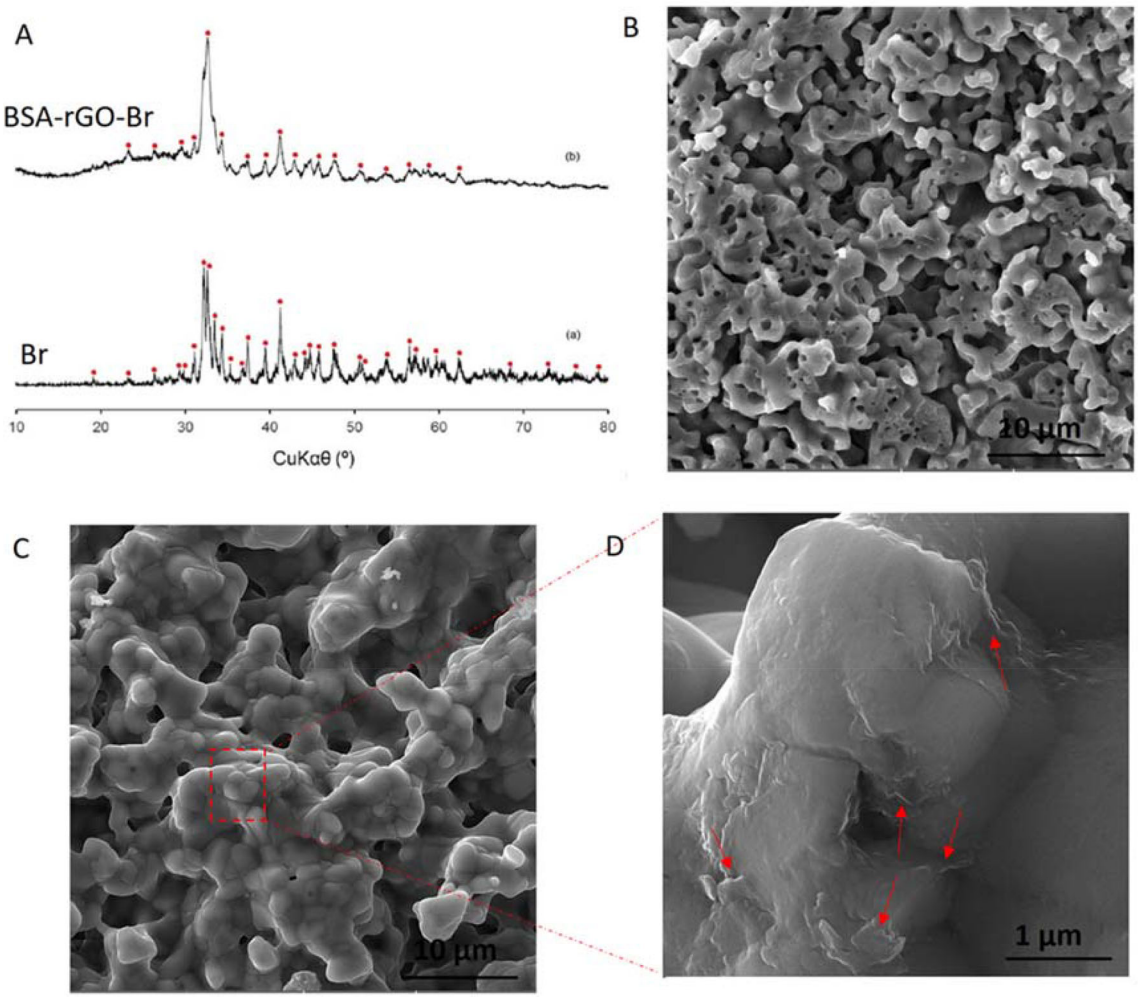

Fig. 5 XRD patterns of Br and BSA-rGO–Br composite (**a**), FESEM images of tablet of Br (**b**), and BSA-rGO–Br tablet (**c** and **d**)

peak, the relatively sharp and broad peak at around 20–27° demonstrates the presence of BSA-rGO in the BSA-rGO–Br nanocomposite XRD pattern [53].

The porosities of the Br and the BSA-rGO are compared in Fig. 5b and c, respectively. In Fig. 5b, the Br is seen to display a bimodal distribution in which the large pores represent the inter-particle gaps and the small pores represent the regions of Br particle agglomeration with decreased inter-particle interactions. By contrast, when the BSA-rGO is introduced to the Br (Fig. 5c), the porosity of the nanocomposite is seen to be significantly decreased. The porous structure of the Br results from the characteristically low thermal conductivity of the bio-ceramic material during the diffusion/densification process. By contrast, the presence of graphene in the BSA-rGO–Br nanocomposite leads to decreased porosity and increased densification due to the better thermal conductivity of graphene. The results in Fig. 5d indicate that the BSA-rGO nanosheets have covered the Br particles and the diffusion/densification process has been successfully completed.

Utilizing elemental mapping test, as a powerful tool to evaluate nanoparticle or nanosheets distribution have been reported previously [57].

The mapping analyses of the BSA-rGO–Br in Fig. 6a–g demonstrate the presence and uniform distribution of the main elements of Br, namely Si, Mg, Ca, and O. Furthermore, a comparison of the EDS spectra in Fig. 6f confirms the presence of Br in the BSA-rGO–Br nanocomposite, while the appearance of carbon in the mapping analyses in Fig. 7a–g confirms the presence of the BSA-rGO nanosheets. Taken together, the presence of carbon in both the mapping and EDS analyses demonstrates the dispersion of the BSA-rGO nanosheets in the Br matrix. Elemental mapping analysis confirms the distribution of BSA-rGO nanosheets in Br matrix. Figure 7h and i shows the EDS spectra of the composite and Fig. 7j demonstrates the statistical analysis of the nanocomposite powder. The results confirm the presence

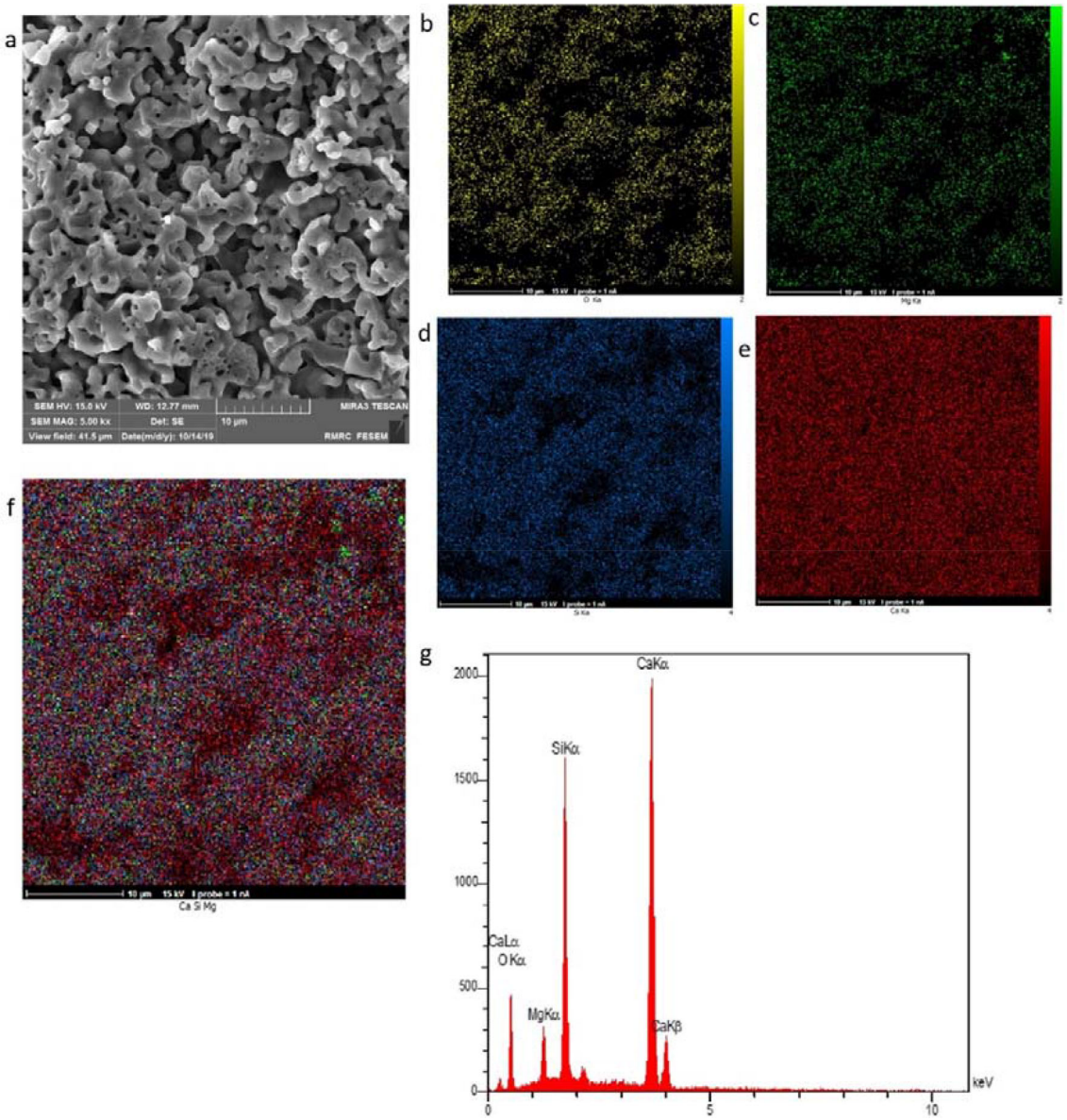

Fig. 6 FESEM image of Br tablet (**a**), elemental mapping and EDS of the Sintered Br Tablet. The O, Mg, Si, and Ca elemental mapping of Br tablets were presented as (**b**), (**c**), (**d**), and (**e**), respectively. In (**f**), distribution of Ca, Si, and Mg are presented as merged pattern. EDS spectrum of Br tablet was shown in (**g**) demonstrating all essential elements exist in the structure

of all essential elements as well as carbon in the structure ($^{*}P < 0.05$ and $^{**}P < 0.1$). The significant relationship between carbon, Mg, and Si is observable in EDS schemes demonstrating that graphene nanosheets are incorporated in the bio-ceramic matrix.

The report by EVANS et al. [58] showed that the hardness of natural bone tissue was found to be considerably higher than that of the analogue materials such hydroxyl appetite polyethylene composite. Enhancing mechanical properties of materials is crucial for using in bone tissue engineering.

The results of the hardness tests for the Br and BSA-rGO–Br are presented in Fig. 8a. Here, the presence of BSA-rGO is seen to significantly increase the microhardness of the nanocomposite. These results demonstrate that even if the concentration of BSA-rGO is low, there is a considerable effect on the bulk mechanical properties. Meanwhile, the comparative microhardness of the Br and BSA-rGO–Br nanocomposite tablets is indicated by the SEM images in Fig. 8b and c, where the width of the indentation-induced crack is seen to be dramatically reduced from 2.6 μm for the Br tablet to 0.4 μm for the BSA-rGO–Br tablet, thus

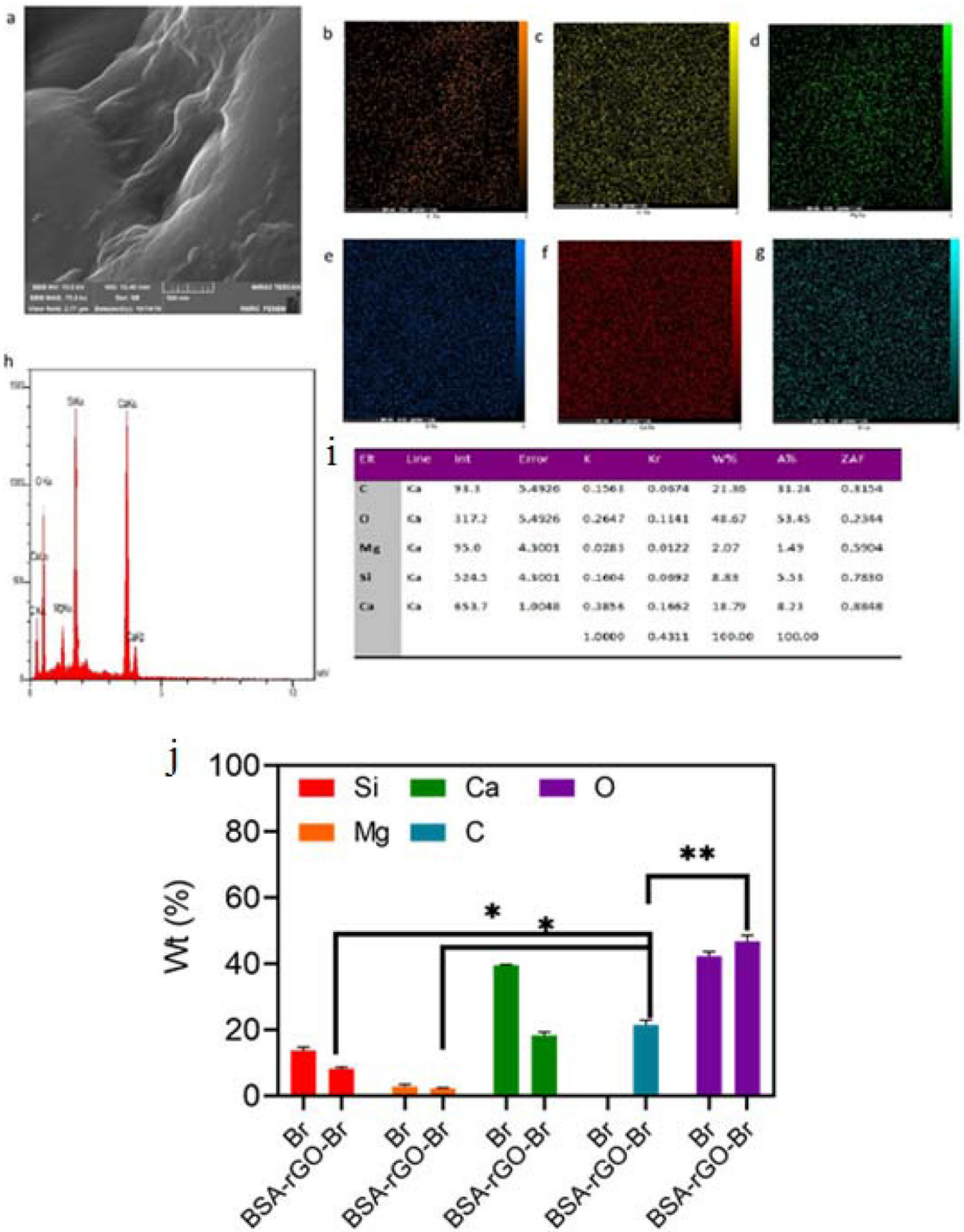

Fig. 7 FESEM image of BSA-rGO–Br powder, which shows semi-homogeneous dispersion of rGO nanosheets (**a**) and EDS elemental mapping of the nanocomposite powders (**b**–**g**). Ca, Si and Mg and C elements are well dispersed on the surface of the nanocomposite powders, representing a homogeneous dispersion of rGO nanosheets in the bio-ceramic. EDS spectrum of the nanocomposite powders (h, i and j) demonstrating all essential elements and carbon in the structure (*$p < 0.05$ and **$P < 0.1$)

demonstrating the enhanced mechanical characteristics of the composite material. These results demonstrate that the addition of BSA-rGO nanosheets can effectively enhance the mechanical properties of the Br bio-ceramic due to better dispersion in the ceramic matrix [59].

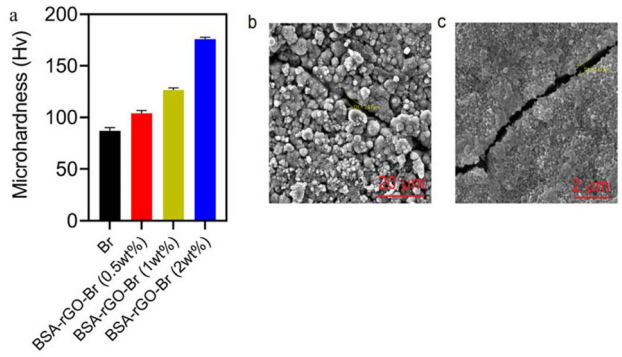

Fig. 8 Quantitative analysis of microhardness (**a**), microhardness SEM of Br tablet (**b**), and microhardness SEM of BSA-rGO–Br composite (**c**)

Br and 2 wt% BSA-rGO-reinforced Br tablets showed adequate anti-washout property (Fig. 9). However, significant differences were observed between 2 wt% BSA-rGO-reinforced Br and pure Br tablets. Br tablets lost 7.1, 12, and 21.1% of initial weight within 12, 24, and 36 h, respectively, while 2 wt% BSA-rGO-reinforced Br had relative improvement in anti-washout property, demonstrating a sufficient anti-washout property as 7.1, 10.1, and 14.3% of first weight within 12, 24, and 36 h, respectively.

Cell culture

One of the interesting properties of graphene-reinforced biomaterials is the enhancement of regeneration capability. Hence, the comparative biocompatibility or toxicity of the Br and BSA-rGO–Br tablets was evaluated by MTT assay to determine the effect of the BSA-rGO nanosheets. After culturing G-292 cells on the surfaces of the various sample tablets for 24 days the optical density (OD) was measured as an indicator of cell viability, and the results are presented in Fig. 10.

Thus, in Fig. 10a, the OD of the 0.5 wt% BSA-rGO–Br tablet was higher than those of the pure Br (control) and the nanocomposites with 1 and 2 wt% BSA-rGO–Br. Moreover, after culturing for 1 week, the 0.5 wt% BSA-rGO–Br nanocomposite continued to show the highest OD of all the samples. BSA-rGO nanosheets have significant effects on the surface and its related properties such as porosity and roughness of tablets. It seems that BSA-rGO in the certain concentration (0.5 wt%) not only enhanced the mechanical properties, but also presented highest cell viability. Favorable surface roughness and pore size in this concentration of BSA-rGO resulted in more cell viability, proliferation, and finally highest OD compared with other samples.

Furthermore, the results in Fig. 10b and c indicate that the quantity of adherent cells is significantly increased by the introduction of graphene into the composite. The G-292 cells are seen to have uniformly covered the surface of the BSA-rGO–Br tablet as a confluent layer, whereas discrete and detached islands are observed on the surface of the pure Br. However, a comparison of the morphology of the adhered cells on the surfaces of the Br and BSA-rGO–Br tablets indicates that the presence of the BSA-rGO does not alter the cell morphology and does not negatively influence the spreading of osteoblast-like cells.

The difference in the quantity of adherent cells on the surfaces of the Br and the nanocomposite demonstrates that the

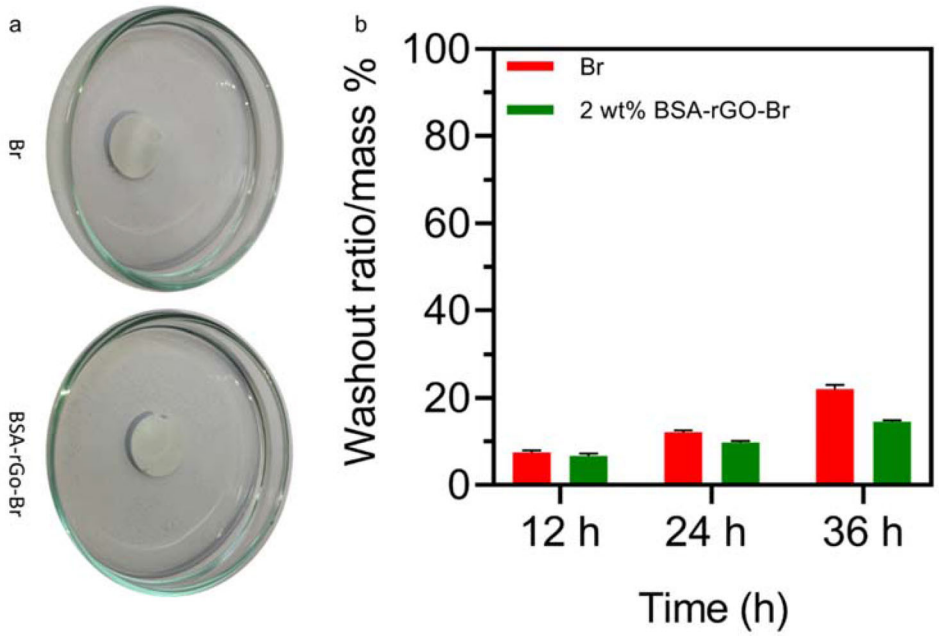

Fig. 9 **a** Photographs after washout property test and **b** washout ratio of Br and 2 wt% BSA-rGO-reinforced Br tablets ($n = 3$)

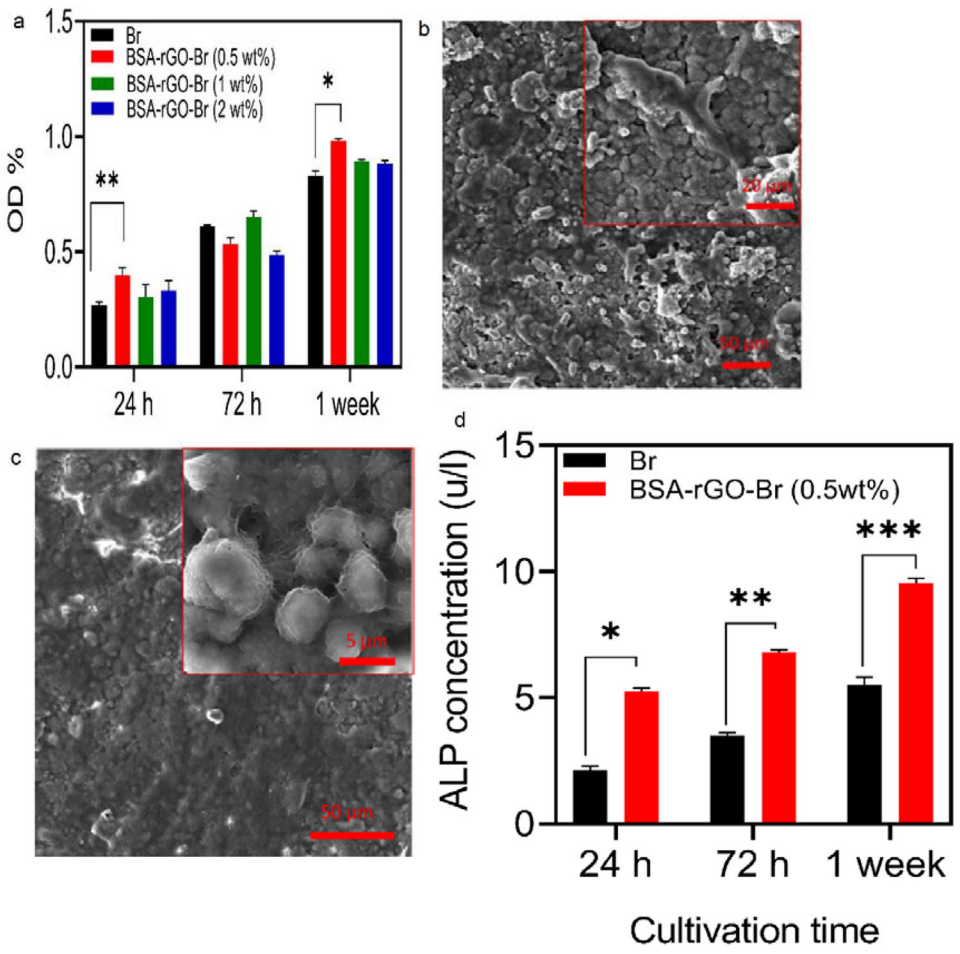

Fig. 10 (**a**) MTT results of Br-rGO nanocomposite: *p-value (0.0003) and **p-value (0.004). SEM images of (**b**) Br tablet and (**c**) Br-rGO composite after cell culture. (**d**) ALP activity of Br tablet and BSA-rGO-Br composite after treatment for 24 h, 72 h, and 1 week: *p-value (0.0003) and **p-value (0.004)

BSA-rGO has a vital influence on the surface-related properties of the bio-ceramic. The results presented in Fig. 10 c and d demonstrate that although the graphene does not significantly affect the dissolution properties of the bio-ceramic, the changes in topography and pore size at the nanoscale induced by the insertion of the wide BSA-rGO nanosheets are essential for the adherence and spread of osteoblasts and related cell lines. It is obvious that BSA-rGO nanosheets enhanced mechanical properties, changed surface roughness and topography of Br tablets and it seems that these are not all of the features that BSA-rGO has been endowed to Br tablets. Surface charge is another feature that is need to be considered and studied in future works. This result is in agreement with the previously reported results relating to graphene-reinforced bio-ceramics [43]. Finally, since it is a crucial feature of osteogenic activity, the alkaline phosphatase (ALP) activity was evaluated for both the Br and the 0.5 wt% BSA-rGO–Br composite. As indicated in Fig. 10d, the cells cultured on the surface of the graphene-reinforced Br displayed a significantly higher ALP than those on the pure Br, thus demonstrating that the introduction of BSA-rGO to the Br matrix enhances the osteogenic bioactivity and osteo-inductivity of both components. Signaling and gene or protein expression in cells are mainly controlled by the surface. Due to different surface properties between Br and BSA-rGO-reinforced Br tablet, ALP activity is different. The differences in the ALP activity or gene expression on the osteoblast cells cultured on the bio-ceramics were reported by our group [49].

Conclusions

Enhancing the mechanical and biological properties of bio-ceramics for bone tissue engineering is crucial. In the present study, the mechanical properties of the bredigite (Br) bio-ceramic were improved by the addition of bovine serum albumin-reduced graphene oxide (BSA-rGO). It was demonstrated that the BSA could effectively reduce the GO nanosheets and provide a suitable interaction between the rGO nanosheets and the Br particles. The uniform dispersion of the BSA-rGO nanosheets in the Br matrix was found to decrease the porosity. The biocompatibility of the nanocomposite was evaluated by MTT assay, which demonstrated that

the addition of graphene did not have a negative effect. The adhesion of G-292 cells was increased by the addition of BSA-rGO nanosheets into the matrix and the ALP activity of the nanocomposite was significantly increased compared to that of the Br tablet, thus demonstrating the excellent osteogenic bioactivity of the synthesized nanocomposite.

Acknowledgements This work is financially supported by Iran University of Science and Technology (IUST) and Motamed Cancer Institute (ACECR).

Author contributions EA, MR and SFD contributed to methodology, investigation and writing original draft. SMN helped in writing-review, editing and validation. YZ helped in writing-review, editing and validation. KYR helped in review and validation.

Compliance with ethics standards

Conflict of interest All authors declare that they have no conflict of interest.

Ethical approval This article does not contain any studies with human or animal subjects performed by any of the authors.

References

1. Zhang B, Sun H, Wu L, Ma L, Xing F, Kong Q et al (2019) 3D printing of calcium phosphate bioceramic with tailored biodegradation rate for skull bone tissue reconstruction. Bio-Design Manuf 2(3):161–171. https://doi.org/10.1007/s42242-019-00046-7
2. Costa JB, Silva-Correia J, Pina S, da Silva A, Vieira S, Pereira H et al (2019) Indirect printing of hierarchical patient-specific scaffolds for meniscus tissue engineering. Bio-Design Manuf 2(4):225–241. https://doi.org/10.1007/s42242-019-00050-x
3. Ansari M, Eshghanmalek M (2019) Biomaterials for repair and regeneration of the cartilage tissue. Bio-Design Manuf 2(1):41–49. https://doi.org/10.1007/s42242-018-0031-0
4. You F, Wu X, Kelly M, Chen X (2020) Bioprinting and in vitro characterization of alginate dialdehyde–gelatin hydrogel bio-ink. Bio-Design Manuf 3(1):48–59. https://doi.org/10.1007/s42242-020-00058-8
5. Dong Y, Duan H, Zhao N, Liu X, Ma Y, Shi X (2018) Three-dimensional printing of β-tricalcium phosphate/calcium silicate composite scaffolds for bone tissue engineering. Bio-Design Manuf 1(2):146–156. https://doi.org/10.1007/s42242-018-0010-5
6. Li X, Yuan Y, Liu L, Leung YS, Chen Y, Guo Y et al (2020) 3D printing of hydroxyapatite/tricalcium phosphate scaffold with hierarchical porous structure for bone regeneration. Bio-Design Manuf 3(1):15–29. https://doi.org/10.1007/s42242-019-00056-5
7. Shao L, Gao Q, Xie C, Fu J, Xiang M, Liu Z et al (2020) Sacrificial microgel-laden bioink-enabled 3D bioprinting of mesoscale pore networks. Bio-Design Manuf 3(1):30–39. https://doi.org/10.1007/s42242-020-00062-y
8. Mehrali M, Moghaddam E, Shirazi SFS, Baradaran S, Mehrali M, Latibari ST et al (2014) Synthesis, mechanical properties, and in vitro biocompatibility with osteoblasts of calcium silicate-reduced graphene oxide composites. ACS Appl Mater Interfaces. 6(6):3947–3962. https://doi.org/10.1021/am500845x
9. Kalantari E, Naghib SM, Reza Naimi-Jamal M, Mozafari M (2017) Green solvent-based sol–gel synthesis of monticellite nanoparticles: a rapid and efficient approach. J Sol-Gel Sci Technol 84(1):87–95. https://doi.org/10.1007/s10971-017-4461-5
10. Fu L, Xiong Y, Carlsson G, Palmer M, Örn S, Zhu W et al (2018) Biodegradable Si3N4 bioceramic sintered with Sr, Mg and Si for spinal fusion: surface characterization and biological evaluation. Appl Mater Today 12:260–275. https://doi.org/10.1016/j.apmt.2018.06.002
11. Zhang Q, Chen L, Chen B, Chen C, Chang J, Xiao Y et al (2019) Lithium-calcium-silicate bioceramics stimulating cementogenic/osteogenic differentiation of periodontal ligament cells and periodontal regeneration. Appl Mater Today 16:375–387. https://doi.org/10.1016/j.apmt.2019.06.011
12. Razavi M, Fathi M, Savabi O, Vashaee D, Tayebi L (2015) Regenerative influence of nanostructured bredigite ($Ca_7MgSi_4O_{16}$)/anodic spark coating on biodegradable AZ91 magnesium alloy implants for bone healing. Mater Lett 155:97–101. https://doi.org/10.1016/j.matlet.2015.04.129
13. Kalantari E, Naghib SM, Naimi-Jamal MR, Aliahmadi A, Iravani NJ, Mozafari M (2018) Nanostructured monticellite for tissue engineering applications - Part I: microstructural and physicochemical characteristics. Ceram Int 44(11):12731–12738. https://doi.org/10.1016/j.ceramint.2018.04.076
14. Kalantari E, Naghib SM, Iravani NJ, Aliahmadi A, Naimi-Jamal MR, Mozafari M (2018) Nanostructured monticellite for tissue engineering applications - Part II: molecular and biological characteristics. Ceram Int 44(12):14704–14711. https://doi.org/10.1016/j.ceramint.2018.05.098
15. Kalantari E, Naghib SM, Naimi-Jamal MR, Esmaeili R, Majidzadeh-A K (2018) Nanostructured monticellite: an emerging player in tissue engineering. Mater Today Proc 5:15744–15753. https://doi.org/10.1016/j.matpr.2018.04.187
16. Wu C, Chang J (2007) Synthesis and in vitro bioactivity of bredigite powders. J Biomater Appl 21(3):251–263. https://doi.org/10.1177/0885328206062360
17. Wu C, Chang J, Wang J, Ni S, Zhai W (2005) Preparation and characteristics of a calcium magnesium silicate (bredigite) bioactive ceramic. Biomaterials 26(16):2925–2931. https://doi.org/10.1016/j.biomaterials.2004.09.019
18. Dezfuli SN, Huan Z, Mol A, Leeflang S, Chang J, Zhou J (2017) Advanced bredigite-containing magnesium-matrix composites for biodegradable bone implant applications. Mater Sci Eng C 79:647–660. https://doi.org/10.1016/j.msec.2017.05.021
19. Askari E, Naghib SM, Seyfoori A, Maleki A, Rahmanian M (2019) Ultrasonic-assisted synthesis and in vitro biological assessments of a novel herceptin-stabilized graphene using three dimensional cell spheroid. Ultrason Sonochem 58:104615. https://doi.org/10.1016/j.ultsonch.2019.104615
20. Rowley-Neale SJ, Randviir EP, Abo Dena AS, Banks CE (2018) An overview of recent applications of reduced graphene oxide as a basis of electroanalytical sensing platforms. Appl Mater Today 10:218–226. https://doi.org/10.1016/j.apmt.2017.11.010
21. Joshi S, Rawat K, C K, Rajamohan V, Mathew AT, Koziol K et al (2020) 4D printing of materials for the future: opportunities and challenges. Appl Mater Today 18:100490. https://doi.org/10.1016/J.APMT.2019.100490
22. Tewari C, Tatrari G, Karakoti M, Pandey S, Pal M, Rana S et al (2019) A simple, eco-friendly and green approach to synthesis of blue photoluminescent potassium-doped graphene oxide from agriculture waste for bio-imaging applications. Mater Sci Eng C 104. https://doi.org/10.1016/j.msec.2019.109970
23. Jurado-Sánchez B, Pacheco M, Maria-Hormigos R, Escarpa A (2017) Perspectives on Janus micromotors: materials and applications. Appl Mater Today 9:407–18. https://doi.org/10.1016/j.apmt.2017.09.005
24. Salahandish R, Ghaffarinejad A, Naghib SM, Majidzadeh-A K, Zargartalebi H, Sanati-Nezhad A (2018) Nano-biosensor for highly

sensitive detection of HER2 positive breast cancer. Biosens Bioelectron 117:104–111. https://doi.org/10.1016/j.bios.2018.05.043
25. Javanbakht S, Namazi H (2018) Doxorubicin loaded carboxymethyl cellulose/graphene quantum dot nanocomposite hydrogel films as a potential anticancer drug delivery system. Mater Sci Eng C 87:50–59. https://doi.org/10.1016/j.msec.2018.02.010
26. Rodrigues RO, Baldi G, Doumett S, Garcia-Hevia L, Gallo J, Bañobre-López M et al (2018) Multifunctional graphene-based magnetic nanocarriers for combined hyperthermia and dual stimuli-responsive drug delivery. Mater Sci Eng C 93:206–217. https://doi.org/10.1016/j.msec.2018.07.060
27. Battogtokh G, Ko YT (2016) Graphene oxide-incorporated pH-responsive folate-albumin-photosensitizer nanocomplex as image-guided dual therapeutics. J Control Release 234:10–20. https://doi.org/10.1016/j.jconrel.2016.05.007
28. Defterali Ç, Verdejo R, Peponi L, Martín ED, Martínez-Murillo R, López-Manchado MÁ et al (2016) Thermally reduced graphene is a permissive material for neurons and astrocytes and de novo neurogenesis in the adult olfactory bulb in vivo. Biomaterials 82:84–93. https://doi.org/10.1016/j.biomaterials.2015.12.010
29. Patel M, Moon HJ, Ko DY, Jeong B (2016) Composite system of graphene oxide and polypeptide thermogel as an injectable 3D scaffold for adipogenic differentiation of tonsil-derived mesenchymal stem cells. ACS Appl Mater Interfaces 8(8):5160–5169. https://doi.org/10.1021/acsami.5b12324
30. Zhang Z, Klausen LH, Chen M, Dong M (2018) Electroactive scaffolds for neurogenesis and myogenesis: graphene-based nanomaterials. Small 14(48). https://doi.org/10.1002/smll.201801983
31. Priyadarsini S, Mohanty S, Mukherjee S, Basu S, Mishra M (2018) Graphene and graphene oxide as nanomaterials for medicine and biology application. J Nanostruct Chem 8(2):123–137. https://doi.org/10.1007/s40097-018-0265-6
32. Martín C, Kostarelos K, Prato M, Bianco A (2019) Biocompatibility and biodegradability of 2D materials: graphene and beyond. Chem Commun 55(39):5540–5546. https://doi.org/10.1039/c9cc01205b
33. Zhou X, Nowicki M, Cui H, Zhu W, Fang X, Miao S et al (2017) 3D bioprinted graphene oxide-incorporated matrix for promoting chondrogenic differentiation of human bone marrow mesenchymal stem cells. Carbon N Y 116:615–624. https://doi.org/10.1016/j.carbon.2017.02.049
34. Liu Y, Wen J, Gao Y, Li T, Wang H, Yan H et al (2018) Antibacterial graphene oxide coatings on polymer substrate. Appl Surf Sci 436:624–630. https://doi.org/10.1016/j.apsusc.2017.12.006
35. Zhang Q, Deng S, Liu J, Zhong X, He J, Chen X et al (2019) Cancer-targeting graphene quantum dots: fluorescence quantum yields, stability, and cell selectivity. Adv Funct Mater 29(5). https://doi.org/10.1002/adfm.201805860
36. Ma R, Tang S, Tan H, Qian J, Lin W, Wang Y et al (2014) Preparation, characterization, in vitro bioactivity, and cellular responses to a polyetheretherketone bioactive composite containing nanocalcium silicate for bone repair. ACS Appl Mater Interfaces 6(15):12214–12225. https://doi.org/10.1021/am504409q
37. Foster CW, Down MP, Zhang Y, Ji X, Rowley-Neale SJ, Smith GC et al (2017) 3D printed graphene based energy storage devices. Sci Rep 7. https://doi.org/10.1038/srep42233
38. Liu J, Yan H, Reece MJ, Jiang K (2012) Toughening of zirconia/alumina composites by the addition of graphene platelets. J Eur Ceram Soc 32(16):4185–4193. https://doi.org/10.1016/j.jeurceramsoc.2012.07.007
39. Yılmaz E, Çakıroğlu B, Gökçe A, Findik F, Gulsoy HO, Gulsoy N et al (2019) Novel hydroxyapatite/graphene oxide/collagen bioactive composite coating on Ti16Nb alloys by electrodeposition. Mater Sci Eng C 101:292–305. https://doi.org/10.1016/j.msec.2019.03.078
40. Cheng Y, Zhang Y, Wan T, Yin Z, Wang J (2017) Mechanical properties and toughening mechanisms of graphene platelets reinforced Al_2O_3/TiC composite ceramic tool materials by microwave sintering. Mater Sci Eng A 680(October):190–196. https://doi.org/10.1016/j.msea.2016.10.100
41. Ramirez C, Miranzo P, Belmonte M, Osendi MI, Poza P, Vega-Diaz SM et al (2014) Extraordinary toughening enhancement and flexural strength in Si_3N_4 composites using graphene sheets. J Eur Ceram Soc 34(2):161–169. https://doi.org/10.1016/j.jeurceramsoc.2013.08.039
42. Li M, Wang Y, Liu Q, Li Q, Cheng Y, Zheng Y et al (2013) In situ synthesis and biocompatibility of nano hydroxyapatite on pristine and chitosan functionalized graphene oxide. J Mater Chem B 1(4):475–484. https://doi.org/10.1039/c2tb00053a
43. Zhang L, Liu W, Yue C, Zhang T, Li P, Xing Z et al (2013) A tough graphene nanosheet/hydroxyapatite composite with improved in vitro biocompatibility. Carbon N Y 61:105–115. https://doi.org/10.1016/j.carbon.2013.04.074
44. Rahmati M, Fathi M, Ahmadian M (2018) Preparation and structural characterization of bioactive bredigite ($Ca_7MgSi_4O_{16}$) nanopowder. J Alloys Compd 732:9–15. https://doi.org/10.1016/j.jallcom.2017.10.132
45. Chen J, Yao B, Li C, Shi G (2013) An improved Hummers method for eco-friendly synthesis of graphene oxide. Carbon N Y 64(1):225–229. https://doi.org/10.1016/j.carbon.2013.07.055
46. Kalantari E, Naghib SM (2019) A comparative study on biological properties of novel nanostructured monticellite-based composites with hydroxyapatite bioceramic. Mater Sci Eng C 98:1087–1096. https://doi.org/10.1016/j.msec.2018.12.140
47. Baradaran S, Moghaddam E, Basirun WJ, Mehrali M, Sookhakian M, Hamdi M et al (2014) Mechanical properties and biomedical applications of a nanotube hydroxyapatite-reduced graphene oxide composite. Carbon N Y 69:32–45. https://doi.org/10.1016/j.carbon.2013.11.054
48. Wu C, Xia L, Han P, Xu M, Fang B, Wang J et al (2015) Graphene-oxide-modified β-tricalcium phosphate bioceramics stimulate in vitro and in vivo osteogenesis. Carbon N Y 93:116–129. https://doi.org/10.1016/j.carbon.2015.04.048
49. Kalantari E, Naghib SM, Iravani NJ, Esmaeili R, Naimi-Jamal MR, Mozafari M (2019) Biocomposites based on hydroxyapatite matrix reinforced with nanostructured monticellite ($CaMgSiO_4$) for biomedical application: synthesis, characterization, and biological studies. Mater Sci Eng C 105. https://doi.org/10.1016/j.msec.2019.109912
50. Mirhadi SM, Tavangarian F, Emadi R (2012) Synthesis, characterization and formation mechanism of single-phase nanostructure bredigite powder. Mater Sci Eng C 32(2):133–139. https://doi.org/10.1016/j.msec.2011.10.007
51. Cihlář J, Buchal A, Trunec M (1999) Kinetics of thermal decomposition of hydroxyapatite bioceramics. J Mater Sci 34(24):6121–6131. https://doi.org/10.1023/A:1004769820545
52. Askari E, Naghib SM (2018) A novel approach to facile synthesis and biosensing of the protein-regulated graphene. Int J Electrochem Sci 13(1):886–897. https://doi.org/10.20964/2018.01.73
53. Yang P, Liu Q, Liu J, Zhang H, Li Z, Li R et al (2017) Bovine serum albumin-coated graphene oxide for effective adsorption of uranium(VI) from aqueous solutions. Ind Eng Chem Res 56(13):3588–3598. https://doi.org/10.1021/acs.iecr.6b04532
54. Childres I, Jauregui LA, Park W, Caoa H, Chena YP (2013) Raman spectroscopy of graphene and related materials. New Dev Phot Mater Res 403–418
55. Liu J, Fu S, Yuan B, Li Y, Deng Z (2010) Toward a universal "adhesive nanosheet" for the assembly of multiple nanoparticles based on a protein-induced reduction/decoration of graphene oxide. J Am Chem Soc 132(21):7279–7281. https://doi.org/10.1021/ja100938r

56. Griep MH, Demaree JD, Cole DP, Henry TC, Karna SP (2020) Protein-mediated synthesis of Au nanocluster decorated reduced graphene oxide: a multifunctional hybrid nano-bio platform. Plasmonics 15(3):897–903. https://doi.org/10.1007/s11468-019-01082-w
57. Shahedi Asl M, Nayebi B, Shokouhimehr M (2018) TEM characterization of spark plasma sintered ZrB_2–SiC–graphene nanocomposite. Ceram Int 44(13):15269–15273. https://doi.org/10.1016/j.ceramint.2018.05.170
58. Evans FG, Vincentelli R (1974) Relations of the compressive properties of human cortical bone to histological structure and calcification. J Biomech 7(1):1–2. https://doi.org/10.1016/0021-9290(74)90064-5
59. Gao C, Feng P, Peng S, Shuai C (2017) Carbon nanotube, graphene and boron nitride nanotube reinforced bioactive ceramics for bone repair. Acta Biomater 61:1–20. https://doi.org/10.1016/j.actbio.2017.05.020